Physica A 391 (2012) 2154–2162

Contents lists available at SciVerse ScienceDirect

Physica A

journal homepage: www.elsevier.com/locate/physa

Tsallis' statistics in the variability of El Niño/Southern Oscillation during the Holocene epoch

Gustavo L. Ferri [a,*], Alejandra Figliola [b], Osvaldo A. Rosso [c,d]

[a] Departamento de Física, Faultad de Ciencias Exactas y Naturales, Universidad Nacional de La Pampa, Uruguay 151, 6300 Santa Rosa, La Pampa, Argentina

[b] Instituto del Desarrollo Humano, Universidad Nacional de General Sarmiento, Juan María Gutiérrez 1150, Los Polvorines, Buenos Aires, Argentina

[c] Departamento de Física, Instituto de Ciências Exatas, Universidade Federal de Minas Gerais, Av. Antônio Carlos, 6627 - Campus Pampulha, 31270-901 Belo Horizonte - MG, Brazil

[d] Chaos & Biology Group, Instituto de Cálculo, Facultad de Ciencias Exactas y Naturales, Universidad de Buenos Aires, Pabellón II, Ciudad Universitaria, 1428 Ciudad Autónoma de Buenos Aires, Argentina

ARTICLE INFO

Article history:
Received 24 August 2011
Available online 26 November 2011

Keywords:
Generalized statistical mechanics
Metastable states
Mixing
Weak chaos
q-triplet
ENSO index

ABSTRACT

Analysis of the Tsallis *q*-triplet for the variability of El Niño Southern Oscillation (ENSO) index during the Holocene epoch (last 11,000 years) is presented. Three periods are analyzed, 0–7000, 7000–9700, 9700–11,000 years before the present. During the first and the third periods, the *q*-index values have the expected usual relations between them ($q_{sens} < 1 < q_{stat} < q_{rel}$), and in the second one there is an inversion between q_{stat} and q_{rel} ($q_{stat} > q_{rel}$).

1. Introduction

The study of climate change throughout the history of Earth has been possible using paleoclimatic data, with records taken from fossil corals, ice sheets, tree rings, sediments, rocks, etc. Climate has been in constant flux for the past few billion years with events ranging from ice ages to long periods of warmth and changes occurring either rapidly (such as ice-sheet disintegration in the poles) or gradually over a long period of time [1]. Studies using paleoclimatic data show that the El Niño/Southern Oscillation (ENSO) has been present in the Earth climate for at least the past 130,000 years [2].

The ENSO system can be thought as a self-sustained oscillator comprising the coupled tropical ocean atmosphere system [3,4]. A sea surface temperature (SST) gradient between the western Pacific warm pool east of Indonesia and the eastern Pacific cold tongue of the Peruvian coast induces the easterly winds of the Walker circulation. These winds in turn stabilize the temperature gradient by driving surface water masses westwards and upwelling of cold deep water close to South America. Perturbations induced by the annual cycle and noise, excite the so-called Kelvin and Rossby waves. Their propagation produce variability on interannual time scales. The El Niño phenomenon sets on in early summer and usually peaks during the winter. It was given the name El Niño, that means in Spanish "the boy", and refers to the Christ child as this periodic warming is seen in the Pacific near South America around Christmas. El Niño events occur every two to seven years and usually cause important socioeconomic impacts. El Niño events are usually followed by a stronger than normal Walker circulation and temperature gradient, called La Niña, the Spanish for "the girl". El Niño and La Niña events are opposite states

* Corresponding author. Tel.: +54 2954 425166.
E-mail addresses: glferri2002@yahoo.com, glferri@exactas.unlpam.edu.ar, gustavoluisferri@gmail.com (G.L. Ferri), alejandra.figliola@gmail.com (A. Figliola), oarosso@fibertel.com.ar (O.A. Rosso).

0378-4371/$ – see front matter © 2011 Elsevier B.V. All rights reserved.
doi:10.1016/j.physa.2011.11.050

of the ENSO system: El Niño occurs when the equatorial Pacific is warmer than average and La Niña occurs when it is cooler than average. Once an El Niño or La Niña event develops, it tends to continue for about a year.

Although there is an increasing number of studies evaluating the behavior of ENSO over millennial time scales, the understanding of its complex dynamics is still limited. Using wavelet analysis on an ENSO proxy record corresponding to the Pallcacocha Lake sedimentary data, Moy et al. [5,6] found a millennial-scale oscillation coherent throughout the Holocene (the present Earth geological era) but displaying less significant variance in the early Holocene. They identified a shift around 5000 before present (BP) from a 1500-yr period in the middle/early Holocene to a 2000-yr period in the late Holocene. Wang and Tsonis [7], Tsonis [8] analyzed this record using several non-linear dynamic techniques and concluded that the shift in behavior around 5000 BP could be explained as a bifurcation in the dynamics given by a transition from chaotic to hyper-chaotic dynamics.

In the present work we continue with the study of the dynamics of the Holocene proxy ENSO record corresponding to the Pallcacocha Lake sedimentary data [5,6], now under the optic of Tsallis' generalized statistical mechanics. In a previous work [9], we analyzed the temporal changes in dynamics over the last 11,000 years, using an entropy Information Theory approach. In that work, we found evidence of a shift in dynamics and cyclic behavior which is consistent with the results of Moy et al. [5]. We also were able to localize these cycles in time and to further analyze possible connections to epochs of rapid climate change (RCC) during the Holocene [10,11].

The present paper is organized as follows: Section 2 gives a brief description of the generalized statistical mechanics used in the present work. The ENSO record corresponding to Pallcacocha Lake sedimentary data is described in Section 3. The Tsallis' q-triplet and its evaluation are described in Sections 4–6, as the corresponding results for the ENSO data are also given. Section 7 contains some final remarks.

2. Special features of generalized statistical mechanics

Generalized statistical mechanics was advanced by Tsallis in 1988 [12,13], as a generalization of the conventional additive Boltzmann–Gibbs statistical mechanics, so that some of its tools could now be used for systems unaccessible before. A particularly important instance is that of systems that find themselves in non-equilibrium but still stationary states, found in a great variety of complex systems. The main Statistical Mechanics-ingredient is the microscopic expression for the entropy in terms of microstates' (labeled by, say, i) probabilities p_i. Instead of the Boltzmann–Gibbs (BG) logarithmic relation:

$$S^{(BG)} = -k \sum_i p_i \ln p_i. \tag{1}$$

Tsallis proposes

$$S_q = -k \left(1 - \sum_i p_i^q \right) \Big/ (1-q), \tag{2}$$

with k standing for Boltzmann's constant. $q \in \mathbb{R}$ is usually referred to as the non-extensivity index. For $q \to 1$, $S_q \to S^{(BG)}$.

The BG conventional statistical mechanics exhibits three main features:

- It leads to a probability distribution function (PDF) describing thermal equilibrium of exponential form in the energy. Thus, the probability of detecting the system in a state of energy u is proportional to $\exp(-\beta u)$.
- Systems well-described à la BG exhibit exponential sensibility to initial conditions. Small initial differences between neighboring states grow in exponential fashion (chaotic dynamics characterized by one or more positive Lyapunov exponents).
- Macroscopic variables exponentially decay to their equilibrium values with a relaxation time τ.

Analogously, Tsallis (or q-)statistics exhibits the following three counterpart-features [14], namely:

(i) Tsallis (or q-)PDF's, that describe meta-stable or stationary states, are proportional to functions called q-exponentials, defined according to

$$\exp_q(-\beta u) = [1 - (1-q)\beta u]^{1/(1-q)}, \tag{3}$$

with β and q constants. In the limit $q \to 1$, q-exponentials become ordinary ones ($\exp_1(x) \equiv \exp(x)$). If $q \to 1$ and $u = y^2$, $\exp_q(-\beta u)$ becomes a q-Gaussian. Stationary states are characterized by a parameter $q \equiv q_{stat}$. The inverse of the q-exponential is the so-called q-logarithm

$$\ln_q(x) = \frac{x^{1-q} - 1}{1-q}. \tag{4}$$

If $q = 1$ then $\ln_1(x) = \ln(x)$ and obviously we have

$$\ln_q[\exp_q(x)] = \exp_q[\ln_q(x)] = 1. \tag{5}$$

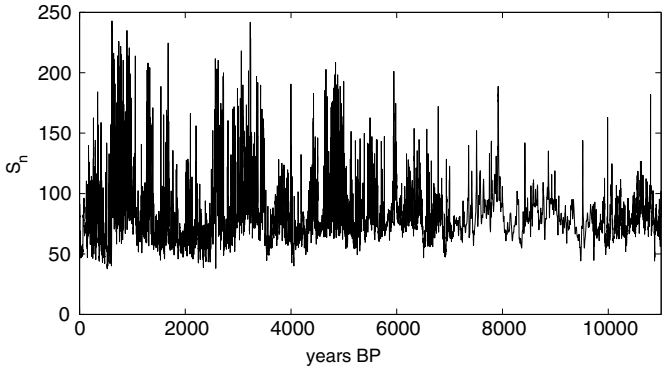

Fig. 1. Time series S_n.

q-Gaussians generalize normal, Gaussian distributions [15], i.e.,

$$G_q(\beta; z) = \frac{\sqrt{\beta}}{C_q} e_q^{-\beta z^2}, \tag{6}$$

where

$$C_q = \frac{\sqrt{\pi}\,\Gamma\left(\frac{3-q}{2(q-1)}\right)}{\sqrt{q-1}\,\Gamma\left(\frac{1}{q-1}\right)} \tag{7}$$

and $1 < q < 3$.

(ii) Stationary states exhibit q-exponential sensibility to initial conditions ("weak" chaos). Small initial differences between neighboring states grow in q-exponential fashion, characterized by a vanishing Lyapunov exponent and a parameter q_{sens}.

(iii) Macroscopic variables q-exponentially decay to their stationary values with $q = q_{rel}$.

Accordingly, a stationary or meta-stable state is characterized by a triplet of q-values (the Tsallis' "q-triplet"), i.e., $(q_{stat}, q_{sens}, q_{rel}) \neq (1, 1, 1)$, where $q_{stat} > 1$, $q_{sen} < 1$, and $q_{rel} > 1$ [14]. As far as we know, just two *empirical* instances of triplet detection have been reported, one of them with reference to the distant helio-magnetic field intensity [16,17] and the other one with reference to the deep of the ozone stratospheric layer [18]. Values for the particular parameter q_{stat} have been reported for the daily variation of the ENSO-index (El Niño Southern Oscillation) [19], and for fluctuations of the cosmic background radiation [20].

3. The El Niño Southern Oscillation data

In the current analysis we study the dynamics of the Holocene proxy ENSO record corresponding to Pallcacocha Lake sedimentary data [5,6]. The proxy record was obtained from the analysis of clastic laminae deposition in sediment two 8-m cores retrieved from the Pallcacocha Lake in Ecuador. Moy et al. [5] explain that during warm ENSO events, convective precipitation triggers erosion and debris-flow activity increasing the sediment load that is contributed to the lake. It was assumed that the light-colored, inorganic clastic sediments laminae in the sediment core were deposited during the ENSO-driven episodes. This hypothesis was based on the observation that light-colored laminae deposited in the more recent 200 years generally correlated with known moderate to severe El Niño events from instrumental and historical records. To quantify the distribution of the light-colored laminae in the lake sediments, the surface of the core sections was digitally scanned and the red color intensity was used to generate the record of ENSO variability. Then, an age model based on radiocarbon chronology was used to create the time series from 11,000 calendar years BP to today of the red color intensity (Holocene period).

As is explained by Moy et al. [5,6], the age-model for the new record is based on the same radiocarbon chronology used by Rodbell et al. [21]. The laminae dated by AMS ^{14}C of terrestrial microfossils in Ref. [21] record are distinctive and could be confidently identified in the new cores. By creating a composite section from overlapping drives, Moy et al. were able to improve on the original age model. They adopted the constant carbon accumulation model and an event model to allocate time between dated intervals [21,22]. The constant carbon accumulation model assumes that the rate of organic carbon deposition has remained nearly constant between radiocarbon-dated intervals through the Holocene, and this continuous sedimentation was punctuated by nearly instantaneous clastic depositional events.

The original Pallcacocha Lake data [6] has been interpolated to a sample time of one year using a cubic Hermite polynomial. The corresponding time series of $M = 11,000$ *data* has been considered in the analysis and is displayed in Fig. 1($T_{sample} = 1$ *year*). Visual inspection of ENSO proxy data from the Pallcacocha Lake, Fig. 1, indicates that during the last 5000 years there is a switch to more frequent and strong El Niño events (high red color intensity).

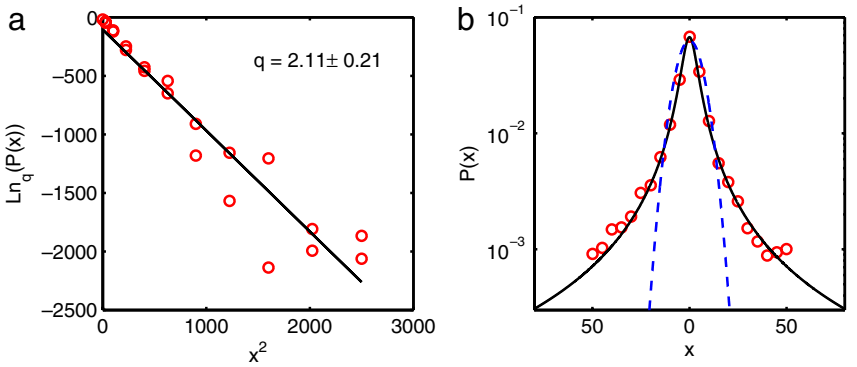

Fig. 2. (a) Linear regression $\ln_q[p\,(x_i)]$ vs. x_i^2 with the q-value that yields the highest CC, corresponding to segment I (0–7000 years BP) of the time series. (b) In circles, the stationary PDF $p\,(x_i)$, and in solid line, the q-Gaussian function that best fits $p\,(x_i)$. The best Gaussian ($q = 1$) function is showed by a dashed line for comparison.

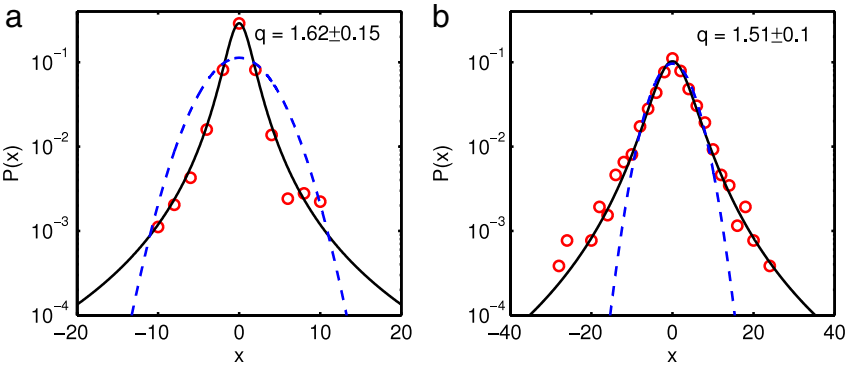

Fig. 3. Same as Fig. 2.b for: (a) segment II (7000–9700 years BP) and (b) segment III (9700–11,000 years BP) of the time series.

In a previous work [9] using the permutation entropy (normalized Shannon entropy evaluated with PDF base on Bandt and Pompe methodology) we were able to point out to varying aspects of the dynamics of the ENSO proxy during the Holocene. Our results indicate that the dynamics of the ENSO proxy record during the rapid climate change (RCC) interval 9000–8000 BP is remarkably different from that of the others RCCs of the Holocene. As explained by Mayewski et al. [11], this RCC interval is the only one that coincides with a significant increase in volcanic aerosol production and it occurred when bipolar ice sheet dynamics still had the potential for substantial effects on global climate. In addition, entropy quantifiers (permutation entropy and also, entropy evaluated with PDF-histograms) point out to the existence of cycles (intervals of increasing and decreasing entropy) with a period close to 2000 years during the mid-to-late Holocene [9].

This cyclic dynamic is consistent with that observed by Moy et al. [5] using wavelet analysis. Taking into account the previous results and in order to perform our analysis based on generalized statistical mechanics of the ENSO proxy data, we have divided the time series into three segments ranging from: (i) 0 to 7000 years BP, (ii) 7000 to 9700 years BP and (iii) 9700 to 11,000 years BP, accordingly with the changes in the entropy described by Saco et al. [9].

4. Stationary $q = q_{stat}$

The suitable q-value for the stationary is obtained from the PDF associated to yearly variations of the ENSO index $\Delta S_n = S_{n+1} - S_n$. The ΔS-range is subdivided into little "cells" of width δx centered at x_i so that one can assess with what frequency ΔS-values fall within each cell. We chose a cell-size $\delta x = 5$ units. The resultant histogram, properly normalized, yields our stationary-PDF $\{p\,(x_i)\}_{i=1}^{N}$. Of course, p_i is the probability for a ΔS-value to fall within the i-th cell, centered at x_i, with N the cell-number.

The graph $\ln_q[p\,(x_i)]$ vs. x_i^2 becomes of interest here (see Fig. 2.a). For a proper assessment we varied q within $[1, 3]$ with $\delta_q = 0.001$, making in each instance a linear adjustment and evaluating the associated correlation coefficient (CC).

In Fig. 2.b the stationary PDF $p\,(x_i)$ corresponding to the first segment of the time series, is showed with circle markers and, with a solid line, the q-Gaussian function that best fits $p\,(x_i)$. For comparison, the best Gaussian fit is also drawn, as a dashed line. The same is showed in Fig. 3(a) and (b) for the second and third segment. Our results for the q_{stat} are summarized in Table 1.

Table 1
Obtained values for the q_{stat}, standard deviation (SD) and the associated correlation coefficient for the three segment considered.

Segment	$q_{stat} \pm \Delta q$	CC
I	2.11 ± 0.21	0.9106
II	1.62 ± 0.15	0.8533
III	1.51 ± 0.10	0.9131

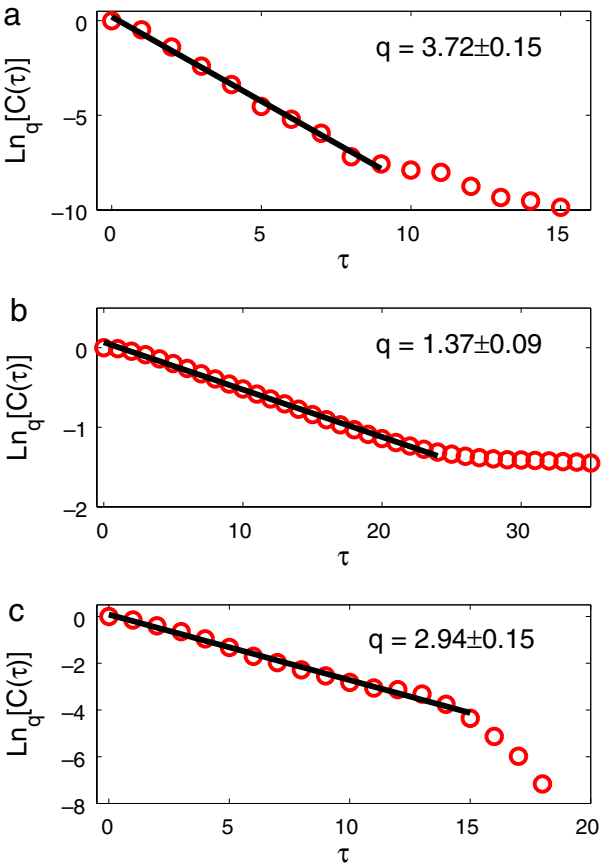

Fig. 4. Linear regression $\ln[C(\tau)]$ vs. τ for (a) segment I (0–7000 years BP); (b) segment II (7000–9700 years BP); (c) segment III (9700–11,000 years BP).

5. Relaxation $q = q_{rel}$

The corresponding q_{rel}-value is determined via the temporal self-correlation coefficient

$$C(\tau) = \frac{\sum_n S_{n+\tau} \cdot S_n}{\sum_n S_n^2}. \tag{8}$$

For a classical BG-process such a correlation should decay in exponential fashion. However we do not find such a behavior. Instead, the self-correlation of our series S_n clearly decays from unity in a q-exponential manner (see Fig. 4. The corresponding values for q_{rel} are given in Table 2.

6. Sensibility to initial conditions $q = q_{sens}$

The q_{sens} can be derived from the multifractal spectrum $f(\alpha)$ of the attractor associated to our nonlinear dynamical system, reflected by S_n. $f(\alpha)$ is the fractal dimension of a spatial cell-subset that contains the attractor, with local-scale exponent α [23]. The spectrum's extremes $\alpha_{\min}$ and $\alpha_{\max}$, for which $f(\alpha) = 0$, are related to q_{sens} [14,24] according to

$$\frac{1}{(1 - q_{sens})} = \frac{1}{\alpha_{\min}} - \frac{1}{\alpha_{\max}}. \tag{9}$$

Table 2
Obtained values for the q_{rel}, standard deviation (SD) and the associated correlation coefficient for the three segments considered.

Segment	$q_{rel} \pm \Delta q$	CC
I	3.72 ± 0.15	0.9949
II	1.37 ± 0.09	0.9967
III	2.94 ± 0.11	0.9916

We have evaluated the multifractal spectrum using the *Multifractal Detrended Fluctuation Analysis* (MFDFA) method, which was presented as a generalization of the Detrended Fluctuation Analysis (DFA) method and it proves its advantage compared with other methods, especially as we deal with non-stationary series, [25–27].

The MFDFA multifractal spectrum estimation of a one-dimensional series $\{x(i), i = 1, \ldots, N\}$ is based on the construction and analysis of the *fluctuation function*, that is defined as:

$$F_s^2(\nu) = \frac{1}{s}\sum_{i=1}^{s}\{Y_s[(\nu-1)s+i]\}^2. \tag{10}$$

To obtain (10) first we calculate the *profile* of the series by the integration: $Y(k) = \sum_{i=1}^{k}[x(i) - \langle x\rangle]$, where $\langle x\rangle$ is the mean value of the series $\{x(i)\}$. The profile is cut into $N_s = N/s$ non-overlapping segments of equal length s. The detrended time series for segment s, denoted by $Y_s(i)$, is calculated as the difference between the original time series and its fit:

$$Y_s(i) = Y(i) - p_\nu(i), \tag{11}$$

where $p_\nu(i)$ is the fitting polynomial in the ν-th segment. Since we use a polynomial fit of order 1, we denote the algorithm as 1-MFDFA, or for simplicity MFDFA. Because the detrending of the time series is done by subtraction of the fits from the profile, these methods differ in their capability of eliminating trends in the data. For each of the N_s segments, the variance of the detrended time series $Y_s(i)$ is evaluated by averaging over all data points i in the ν-th segment. Then, averaging over all segments, it is possible to obtain the g-th fluctuation function:

$$F_g(s) = \left\{\frac{1}{2N_s}\sum_{\nu=1}^{2N_s}\left[F_s^2(\nu)\right]^{g/2}\right\}^{1/g}, \tag{12}$$

where, in general, the index g can take any real value. For $g = 2$, the standard DFA procedure is retrieved. The scaling behavior of the fluctuation function is determined by analyzing log–log plots $F_g(s)$ versus s for each value of g. If the series $x(i)$ is long-range power-low correlated $F_g(s)$ increases, for large values of s, as a power-law:

$$F_g(s) \sim s^{h(g)}. \tag{13}$$

For more details see Ref. [25].

For monofractal time series with compact support, $h(g)$ is independent of g, since the scaling behavior of the variance $F_s^2(\nu)$ is identical for all segments ν and the averaging procedure in Eq. (12) will give just this identical scaling behavior for all values of g. Only if small and large fluctuations scale differently, will there be a significant dependence of $h(g)$ on g. If we consider positive values of g, the segments ν with large variance $F_s^2(\nu)$ will dominate the average $F_g(s)$. Thus, for positive values of g, $h(g)$ describes the scaling behavior of the segments with large fluctuations. On the contrary, for negative values of g, the segments ν with small variance $F_s^2(\nu)$ will dominate the average $F_g(s)$. Hence, for negative values of g, $h(g)$ describes the scaling behavior of the segments with small fluctuations and it is known as the *generalized Hurst exponent*. When $g = 2$, the $h(2)$ is the *Hurst exponent*.

Following from Eqs. (12) to (13) and assuming that the length N of the series is an integer multiple of the scale s,

$$\sum_{\nu=1}^{N/s}|Y(\nu s) - Y((\nu-1)s)|^g \sim s^{gh(g)-1}. \tag{14}$$

Kantelhardt and co-workers show that this multifractal formalism corresponds with the standard box counting theory and they related both formalisms. It is obvious that the term $|Y(\nu s) - Y((\nu-1)s)|$ is identical to the sum of the numbers $x(i)$ within each segment ν of size s. This sum is the box probability $p_s(\nu)$ in the standard formalism for normalized series $x(i)$ [25].

The scaling function $\eta(g)$ is usually defined from last equation:

$$\eta(g) = g\,h(g) - 1 \tag{15}$$

where g is a real parameter. The Hölder exponents α and the multifractal spectrum $f(\alpha)$ are related with $\eta(g)$ via a Legendre transform, in the case that $\eta(g)$ is concave, Ref. [28]:

$$\alpha = \eta'(g) \tag{16}$$

Table 3
Obtained values for the q_{sens}, standard deviation (SD) and the associated correlation coefficient for the three segment considered.

Segment	$\alpha_{max} \pm \Delta\alpha_{max}$	$\alpha_{min} \pm \Delta\alpha_{min}$	$q_{sens} \pm \Delta q$
I	0.996 ± 0.0122	0.289 ± 0.0083	0.592 ± 0.049
II	1.538 ± 0.0234	0.502 ± 0.0128	0.256 ± 0.083
III	1.612 ± 0.0237	0.498 ± 0.0159	0.279 ± 0.095

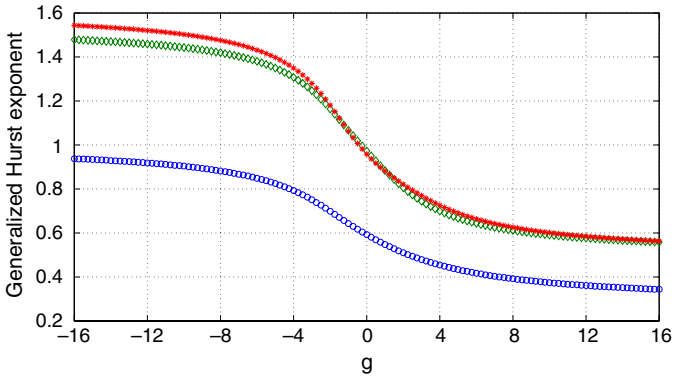

Fig. 5. Generalized Hurst exponent for the three segments. Circles correspond to segment I (0–7000 years BP), diamonds to segment II (7000–9700 years BP) and asterisks to segment III (9700–11,000 years BP).

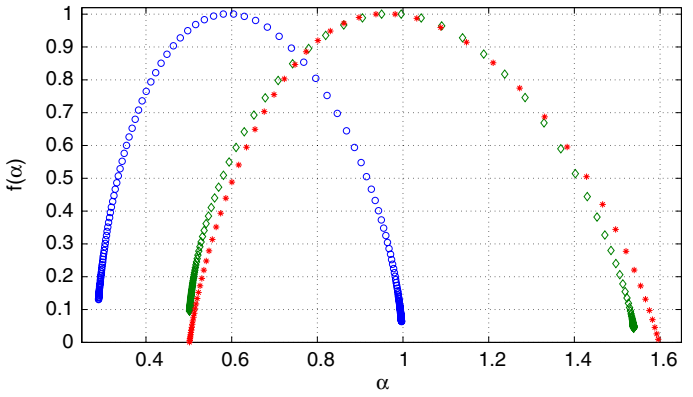

Fig. 6. Multifractal spectrum for the three segments. Circles correspond to segment I (0–7000 years BP), diamonds to segment II (7000–9700 years BP) and asterisks to segment III (9700–11,000 years BP). Note the significant difference between the spectra from segment I and segment II and III.

and

$$f(\alpha) = g\,h - \eta(g). \tag{17}$$

Then, MFDFA can be framed into the multifractal formalism. In multifractal systems, the strength of multifractality can be described by the width of the spectrum $\Delta\alpha$. It is easy to show that: $\alpha_{max} = h(-\infty)$ and $\alpha_{min} = h(+\infty)$. So, to estimate α_{max} and α_{min} can use the function $h(g)$ with $|g| \gg 1$.

The MFDFA method for calculating q_{sens} is the easy implementation, avoids numerical errors introduced by the numerical calculation of derivatives and is optimal in the case of highly non-stationary series as the one presented. In Fig. 5 we present the Generalized Hurst exponent $h(g)$ for the three periods and in Fig. 6 the corresponding Multifractal Spectrum obtained from Eqs. (16) to (17). Fig. 7 shows the results for the *Fluctuation function* ($F_g(s)$) and its fitting for the three segments and the two cases ($\alpha_{max} = h(-\infty)$ and $\alpha_{min} = h(+\infty)$), as explained by Mayewski et al. [11]. The obtained values for q_{rel} are given in Table 3.

7. Final remarks

In this paper we report the values of the Tsallis-nonextensivity triplet for ENSO during the Holocene epoch based on the record corresponding to the Pallcacocha Lake sedimentary data. We divided the record in three periods as reported in a previous work [9] corresponding to different dynamics. In Fig. 8 we summarize our results for q-triplets corresponding to the

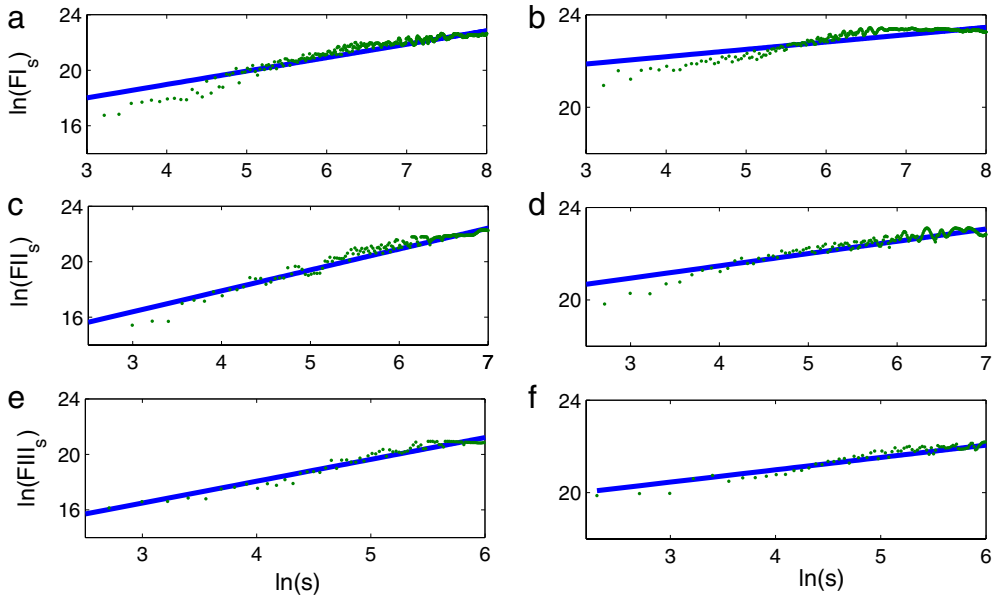

Fig. 7. $\ln(F_g(s))$ vs. $\ln(s)$ for the three segments and the two cases ($\alpha_{\max} = h(-\infty)$ and $\alpha_{\min} = h(+\infty)$). The slope of the fitted line by the data correspond to the values of $h_{\max} = h(-\infty)$ and $h_{\min} = h(+\infty)$ respectively. (a) and (b) correspond to segment I (0–7000 years BP) for $h_{\max}$ and $h_{\min}$ respectively, (c) and (d) for segment II (7000–9700 years BP) and (e) and (f) for segment III (9700–11,000 years BP).

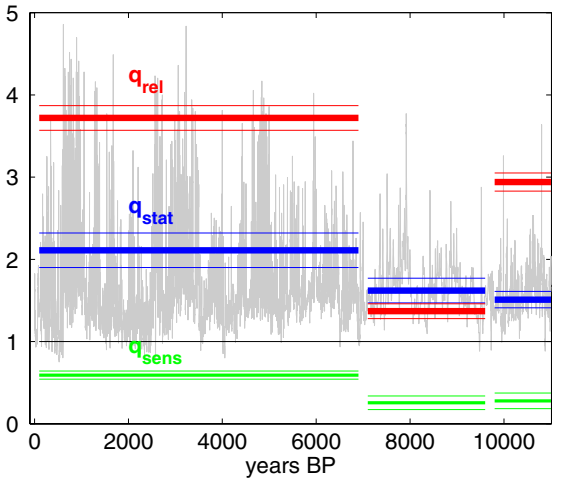

Fig. 8. q-triplet values with error bars, corresponding to the three periods analyzed.

three periods considered. For these periods we conclude that: Segments I and III meet the inequality $q_{sens} < 1 < q_{stat} < q_{rel}$ and segment II reverses the relationship between q_{stat} and q_{rel}, and it results in $q_{stat} > q_{rel}$. It is interesting to remark that this is the first time that this inversion is observed. We understand that this is a clear manifestation of the change in the dynamic of ENSO recording during the Rapid Climatic Change (RCC) in the interval 8000–9000 years BP, consistent with previous works based on wavelet analysis [5,6] and entropy analysis [9]. As explained by Mayewski et al. [11], this RCC interval in the only one that coincides with a significant increased in volcanic aerosol production, and it occurred when bipolar ice sheet dynamics still had the potential for substantial effects on global climate. Also, from the multifractal formalism we can observe the difference of the Generalized Hurst exponent (Fig. 5) and the Multifractal Spectrum (Fig. 6) between the data from period II and the data corresponding to periods I and III.

Acknowledgments

A. Figliola and O. A. Rosso acknowledge partial support from the Consejo Nacional de Investigaciones Científicas y Técnicas (CONICET), Argentina. Gustavo Ferri thanks to the UNLPam. OAR gratefully acknowledges support from CAPES, PVE fellowship, Brazil and A. F. thanks the UNGS.

References

[1] M. Das, S. Parthasarathy, Anomaly detection and spatio–temporal analysis of global climate system, in: Proceedings of the Third International Workshop on Knowledge Discovery from Sensor Data, Paris, 2009, pp. 142–150.
[2] M.A. Cane, The evolution of El Niño, past and future, Earth an Planetary Science Letters 164 (2004) 1–10.
[3] D. Maraun, What can we learn from climate data? methods for fluctuation, time/scale and phase analysis, Ph.D. Thesis, University of Potsdam, Potsdam, Germany, 2006, p. 62.
[4] J. Bjerknes, Atmospheric teleconnections from the equatorial Pacific, Mon. Wea. Rev. 97 (1969) 163–172.
[5] C.M. Moy, G.O. Seltzer, D.T. Rodbell, D.M. Anderson, Variability of El Niño Southern Oscillation activity at millennial timescales during the Holocene epoch, Nature 420 (2002) 162–165.
[6] C.M. Moy, G.O. Seltzer, D.T. Rodbell, D.M. Anderson, Laguna Pallcacocha sediment color intensity data, IGBP PAGES/World Data Center for Paleoclimatology Data Contribution Series 2002–76, NOAA/NCDC Paleoclimatology Program, Boulder CO, 2002. Data available online at: http://www.ngdc.noaa.gov/paleo/pubs/moy2002.
[7] G. Wang, A.A. Tsonis, On the variability of ENSO at millennial timescales, Geophysical Research Letters 35 (2008) L17702.
[8] A.A. Tsonis, Dynamical changes in the ENSO system in the last 11,000 years, Clymate Dynamics 33 (2008) 1069–1074.
[9] P.M. Saco, L.C. Carpi, A. Figliola, E. Serrano, O.A. Rosso, Entropy analysis of the dynamics of El Nio/Southern Oscillation during the Holocene, Physica A 389 (2010) 5022–5027.
[10] G.H. Denton, W. Karlén, Holocene climatic variations: their pattern and possible cause, Quaternary Research 3 (1973) 155–205.
[11] P.A. Mayewski, E.E. Rohling, J.C. Stanger, W. Karlén, K.A. Maasch, L.D. Meeker, E.A. Meyerson, F. Gasse, S. van Kreveld, K. Holmgren, J. Lee-Thorp, G. Rosqvist, F. Rack, M. Staubwasser, R.R. Schneider, E. Steig, Holocene climate variability, Quaternary Research 62 (2004) 243–255, and references therein.
[12] C. Tsallis, A possible generalization of Boltzmann–Gibbs entropy, J. Stat. Phys. 52 (1988) 479–486.
[13] C. Tsallis, Introduction to Nonextensive Statistical Mechanics—Approaching a Complex World, Springer, New York, 2009.
[14] C. Tsallis, Dynamical scenario for nonextensive statistical mechanics, Physica A 340 (2004) 1–10.
[15] S. Umarov, C. Tsallis, S. Steinberg, Generalization of the central limit theorem consistent with non-extensive statistical mechanics. http://arxiv.org/abs/cond-mat/0603593v4, 2007.
[16] L.F. Burlaga, A.F. Viñas, Triangle for the entropic index q of non-extensive statistical mechanics observed by Voyager I in distant heliosphere, Physica A 361 (2006) 173–179.
[17] L.F. Burlaga, A.F. Viñas, N.F. Ness, M.H. Acuña, Tsallis statistics of the magnetic field in the heliosheath, The Astrophisical Journal 644 (2006) L83–L86.
[18] G.L. Ferri, M.F. Reynoso Savio, A. Plastino, Tsallis q-triplet and the ozone layer, Phisica A 389 (2010) 1829–1833.
[19] F. Petroni, M. Ausloos, High frequency daily data analysis of the Southern Oscillation Index, Tsallis nonextensive statistical mechanics approach, European Physical Journal Special Topics 143 (2007) 201–208.
[20] A. Bernui, C. Tsallis, Thyrso Villela, Temperature fluctuations of the cosmic microwave background radiation: A case of non-extensivity? Physics Letter A 356 (2006) 426–430.
[21] D.T. Rodbell, G.O. Seltzer, D.M. Anderson, M.B. Abbott, D.B. Enfield, J.H. Newman, An ∼15,000-year record of El Nino-driven alluviation in southwestern Ecuador, Science 283 (1999) 516–520.
[22] C.M. Moy, A continuous record of Late-Quaternary El Nino-Southern oscillation from the Southern Ecuadorian Andes, MS Thesis, Syracuse University, 2000.
[23] C. Beck, F. Schlögl, Thermodynamics of chaotic systems, an introduction, in: Cambridge Nonlinear Science Series, Cambridge University Press, 1993.
[24] M.L. Lyra, C. Tsallis, Nonextensivity and multifractality in low-dimensional dissipative systems, Phys. Rev. Lett. 80 (1998) 53–56.
[25] J.W. Kantelhardt, S.A. Zschiegner, E. Koscielny-Bunde, S. Havlin, A. Bunde, H.E. Stanley, Multifractal detrended fluctuation analysis of nonstationary time series, Physica A 316 (2002) 87–114.
[26] E. Serrano, A. Figliola, Wavelet leaders: a new method to estimate the multifractal singularity spectra, Physica A 388 (2009) 2793–2805.
[27] P. Oświęcimka, J. Kwapień, S. Drożdż, Wavelet modulo maxima versus detrended fluctuation analysis of multifractal structures, Phys. Rev. E 74 (2006) 8–17.
[28] K. Falconer, Techniques in Fractal Geometry, John Wiley and Sons Ltd., New York, 1997.